Medium Range Ordering in the Ionic Glass Electrolytes LiPON and LiSiPON

Andrew S. Westover,[1]* Mordechai Kornbluth,[2] Takeshi Egami,[3,4] Jue Liu,[5] Sergiy Kalnaus,[6] Dong Ma,[5,7] Andrew K. Kercher, [1] Joerg C. Neuefeind,[5] Michelle Everett,[5] Victor Torres,[8] Steve Martin,[8] Boris Kozinsky,[9,2] Nancy J. Dudney[1]

[1]Chemical Sciences Division, Oak Ridge National Laboratory, Oak Ridge, TN 37831, USA

[2] Robert Bosch Research and Technology Center, Cambridge, MA 02139, USA

[3]Department of Materials Science and Engineering, and Department of Physics and Astronomy, University of Tennessee, Knoxville, Tennessee 37996, USA

[4]Materials Sciences and Technology Division, Oak Ridge National Laboratory, Oak Ridge, Tennessee 37831, USA

[5]Neutron Sciences Division, Oak Ridge National Laboratory, Oak Ridge, TN 37831, USA

[6]Computational Sciences and Engineering Division, Oak Ridge National Laboratory, Oak Ridge, TN 37831-6164, USA.

[7]Neutron Science Platform, Songshan Materials Laboratory Lake, Dongguan, Guangdong 532800, China

[8]Department of Materials Science and Engineering, Iowa State University, Ames, IA 50011, USA

[9]John A. Paulson School of Engineering and Applied Sciences, Harvard University, Cambridge, Massachusetts 02138, USA

*Corresponding authors emails: westoveras@ornl.gov

TOC Image

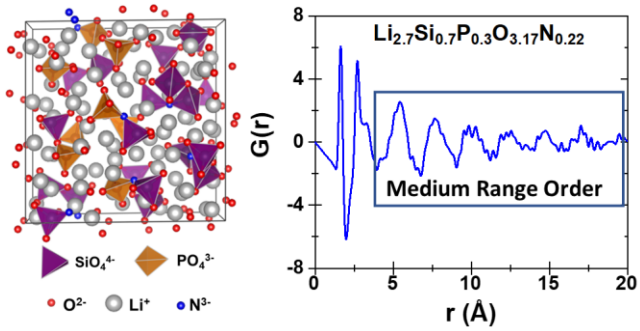

ABSTRACT:

Here we provide an in-depth structural characterization of the amorphous ionic glasses LiPON and LiSiPON with high Li content. Based on ab-initio molecular dynamics simulations, the structure of these materials is an inverted structure with either isolated polyanion tetrahedra or polyanion dimers in a Li^+ matrix. Based on neutron scattering data, this type of inverted structure leads to a significant amount of medium-range ordering in the structure, as demonstrated by two sharp diffraction peaks and a periodic structural oscillation in the density function $G(r)$. While this medium range ordering is commonly observed in liquids and metallic glasses, it has not previously been observed in oxides. On a local scale, adding N and Si increases the number of anion bridges and polyanion dimer structures, leading to higher ionic conductivity. In the medium range ordering, the addition of Si leads to more disorder in the polyanion substructure but a significant increase in the ordering of the O substructure. Finally, we demonstrate that this inverted structure with

medium range ordering results in a glassy material that is both mechanically stiff and ductile on the nanoscale.

INTRODUCTION:

Amorphous materials are critical to numerous technologies.[1] While amorphous materials play a critical role in our society, the structure of amorphous materials is often difficult to define and characterize.[1-2] This is true even for the most common amorphous materials such as SiO_2.[3-4] Despite the difficulty in characterization, the structure of these materials is often integral to their properties and applications.[5-6] One example is the amorphous material lithium phosphorus oxynitride or LiPON which represents a large range of compositions. Sputtered versions of LiPON with high alkali content have been an important battery material for the last three decades.[7-10] This material can remarkably suppress Li dendrite formation, one of the key obstacles to using high energy density Li metal anodes.[11-12] Furthermore, this nominally hard and rigid electrolyte can accommodate volume expansions and contractions that a cathode exhibits during charging and discharging without capacity loss. While the effectiveness of the material is clear, the structural origin to its key properties is less so.

Efforts to understand the structure of LiPON date back to its discovery in the early 1990s. Initial efforts relied on X-ray photoelectron spectroscopy (XPS), Raman spectroscopy, infrared spectroscopy (IR), and nuclear magnetic resonance (NMR).[13] [14-15] Many of these investigations have centered around the effect of substituting N into the amorphous Li_3PO_4 structure. Based on XPS similarities with low alkali phosphate glass, some researchers came to the faulty assumption that N forms primarily double and triple bridges. Recently, Lacivita *et al.* published a paper that used ab-initio molecular dynamics (AIMD) simulations in conjunction with experimental neutron scattering and IR measurements to determine the role of this N.[16-17] This work found that for high Li contents, the N is incorporated into the structure as apical (non-bridging) and bridging N. Valentina et al. also found a correlation between the amount of bridging N and ionic conductivity.

One of the drawbacks with LiPON has been relatively low ionic conductivity on the order of ~10^{-6} S/cm.[16] Recently Si-doped and Si dominant variants of LiPON known as LiSiPON have been demonstrated to have higher ionic conductivity in the range of ~10^{-5} S/cm.[18-20] These LiSiPON materials appear to have a similar capability to prevent Li dendrite formation and enable thin film batteries with Li metal. While substituting P for Si significantly improves the ionic conductivity, the structural origin of this ionic conductivity improvement has yet to be determined.

Even though the local structure previously determined for LiPON seems to have a significant impact on ionic conductivity, the origin of LiPON's ability to mitigate Li penetration is still unclear. A recent study of the mechanics of LiPON using nanoindentation found that LiPON has an unusually high resistance to fracture predicated on the ability to deform plastically on the nano and microscale.[21] LiPON also recovers

deformation over time, which is not typical of ceramics.[21-22] These unusual mechanics cannot be explained based on the local structure alone. A clear understanding of the medium-range ordering from 5-30 Å could provide significant insight into the mechanics of LiPON and similar amorphous ceramics. In previous works, this medium-range ordering was overlooked.

Building on the prior work by Lacivita *et al.,*[16], this work presents a combined ab-initio and neutron scattering study on LiPON and LiSiPON materials. While the prior work was focused purely on the short-range ordering of the LiPON material, this work provides a comprehensive look at the effect of Si substitution on the local structure of the LiPON as well as a detailed look at some of the medium-range ordering from 5-25 Å. The data for the short range order clearly shows that the addition of Si increases the propensity to form anion bridges for a given Li:polyanion ratio likely resulting in higher ionic conductivity. In the medium range order, a clear oscillation in the density function G(r) is observed. While the full impact of this oscillation is still unclear, the materials with this medium range order clearly exhibit superior ionic conductivity and mechanically ductility when compared with traditional metaphosphate glasses.

RESULTS

In the work of Lacivita et al.,[16] simulated LiPON structures exhibited N in either apical or bridging configurations depending on the Li and N content in the structures. They also simulated motion in and around the apical and bridging N and found that Li^+ moves faster near bridging N. These results were in direct alignment with a survey of all experimental results for LiPON in the literature that shows a peak in ionic conductivity with a Li:P ratio of 2.9:1. Coincidentally, this is about the Li:P ratio at which N transitions from being

predominately bridging N to being predominantly apical N. Based on this data, Lacivita et al. argued that the presence of anion bridges at higher Li content is key to improving ionic conductivity when N is substituted into the amorphous Li_3PO_4 structure. Si doping has recently been shown to significantly increase the ionic conductivity up to ~10^{-5} S/cm.[20] One possible explanation for this improved ionic conductivity could be the number of anion bridges. The first goal of this study was to provide more insight into the local structure of LiPON, especially with the addition of Si.

To estimate the number of anion bridges, we used ab-initio molecular dynamics (AIMD) to simulate multiple amorphous structures, including $LiPO_3$, $Li_4P_2O_7$, Li_3PO_4, $Li_{2.7}PO_{3.52}N_{0.22}$, $Li_{2.11}Si_{0.66}P_{0.33}O_{2.93}N_{18}$, $Li_{2.7}Si_{0.7}P_{0.3}O_{3.17}N_{0.22}$, and $Li_{3.7}Si_{0.5}P_{0.5}O_{3.5}N_{0.4}$. Visual representations of three structures, $LiPO_3$, $Li_{2.7}PO_{3.52}N_{0.22}$, and $Li_{2.7}Si_{0.7}P_{0.3}O_{3.17}N_{0.22}$, are shown in Figure 1. The structure across this compositional space ranges from long network phosphate chains connected by a significant amount of bridging O in $LiPO_3$ to a completely inverted structure for Li_3PO_4. This inverted glass structure consists of phosphate polyanions in a Li^+ matrix. In this structure, there is no bridging O. N incorporation results in a few N bridges producing a small number of tethered phosphate dimers $P_2O_6N^{5-}$. When Si is included in the structure, the number of connected polyanions increases further. One reason for this is that for a given Li:polyanion ratio, the lower 4^+ oxidation state of Si vs. 5^+ oxidation state of P means anion bridges are needed to balance the charge. For silicates, a fully inverted structure requires Li_4SiO_4.

To give some experimental confirmation of the quality of the modeled structures, selected comparisons of the local (1-6 Å) structure pair distributions functions (PDFs), $g(r)$, for $Li_{2.7}PO_{3.52}N_{0.22}$ and $Li_{2.7}Si_{0.7}P_{0.3}O_{3.17}N_{0.22}$ are presented in Figure 1 d-e, as $G(r)$ =

$4\pi r\rho_0[g(r) - 1]$, where ρ_0 is the atomic number density. The same comparison for $LiPO_3$ is presented in Figure S1. The PDF describes the distribution of distances between atoms. The first key thing to note is the excellent agreement between the experimental and simulated PDF, with observed discrepancies likely arising from the difficulty in accurately characterizing the exact composition of experimentally synthesized materials. Despite this discrepancy, the total anion:P ratio, which is what governs the connectivity structure of the phosphate network, is 3.77 in simulation and 3.75 in experiment, well within the error tolerances of both methods. For LiPON, the peak intensities and peak shapes match very well for the first peaks at 1.60 Å (P-O & P-N), 1.94 Å (Li-O), 2.24 Å (Li-N), and 2.60 Å (O-O, N-N, & O-N). Beyond 3 Å, there is still good agreement showing a large broad O-O correlation peak between 4-6 Å. As the modeled composition is $Li_{2.7}PO_{3.52}N_{0.22,}$ and the experimental composition is estimated to be $Li_{2.9}PO_{3.85}N_{0.40,}$ it is not surprising that some minor discrepancies occur.

The pair distribution function of the LiSiPON materials shows a similar structure to LiPON, with the first peak at 1.63 Å corresponding to the first cation-anion coordination, including Si-O, Si-N, P-O, and P-N. Because the specific peaks are so close together, it is impossible to distinguish them without a deconvolution. This first peak is followed by the Li-O and Li-N peaks at 1.95 Å and 2.37 Å, respectively, and a peak at 2.72 Å corresponding to the O-O, N-O, and N-N. Again, these are too close together to deconvolute. Both the Si, P-O/P-N peaks and the O-N/O-O/N-N peaks are slightly shifted to larger radial lengths as expected due to the slightly longer Si-O and Si-N bond lengths compared to the P-O and P-N. In this local region, the most significant discrepancies between experimental and simulated PDF are the peak intensities for the first few peaks and an enhanced peak in the

experimental model at 3.1 Å. These discrepancies, again, likely arise due to the difficulty and associated error in getting the exact elemental composition of the material. The enhanced peak at 3.1 Å is indicative of an O-O correlation that is absent in both the N-N and N-O partial pair distribution functions. An overestimate in the N content and underestimate of the O content would likely account for this difference (see Figure S2). The exact details of the compositional analysis are presented in a prior publication.

Figure 1f presents the simulated partial PDF for cation (Si, P) to cation (Si, P) interactions. This cation-cation partial PDF gives insight into the number of bridging anions in the structures demonstrated by the peak that ranges between 2.5-3.5 Å. These partial PDF data clearly show that for $LiPO_3$, there are a significant number of O bridges, but for Li_3PO_4, the bridging cation-cation peak at 2.9 Å is nonexistent. This observation directly matches the expected number of P-O-P bridges based on a compositional assessment, as seen in Figure 1g. The dotted black line represents the expected number of bridging anions for a given composition, and the black dots are the simulated lithium phosphate compositions. The black dots almost perfectly lie on the dotted black line. When N is doped into the structure to make $Li_{2.7}PO_{3.52}N_{0.22,}$ the bridging cation-cation peak at 2.9 Å is clearly present. In Figure 1f, the red dot represents this LiPON datapoint. Based on the prior work, adding N increases the number of bridging anions relative to the expected pure oxide lithium phosphate compositions.

For the Si-doped structures, the analysis of the structure becomes more complex. With the same Li-cation ratio as for the prior $Li_{2.7}PO_{3.52}N_{0.22}$ structure, in $Li_{2.7}Si_{0.7}P_{0.3}O_{3.17}N_{0.22}$, the cation-cation peaks are also present. For $Li_{2.7}Si_{0.7}P_{0.3}O_{3.17}N_{0.22,}$ the cation-cation peak corresponding to the dimers occurs at 3.1 Å and is higher in intensity than for

$Li_{2.7}PO_{3.52}N_{0.22}$. When comparing to the expected LiSiPON structures, Figure 1f reveals that the Si-doped structures have significantly more bridging anions than expected for any given Li: Si+P ratio. In this figure, the blue dotted line is the expected number of bridging anions based on a Si:P ratio of 0.5:0.5. The green dotted line is the expected number of bridging anions for the pure lithium orthosilicate structure. Notably, the number of bridging anions in the simulated structure is greater than expected for the pure silicate compositions. This observation predominantly occurs due to the incorporation of N. The isolated lithia may also be an artifact of the modeling and not an accurate representation of experimental samples.

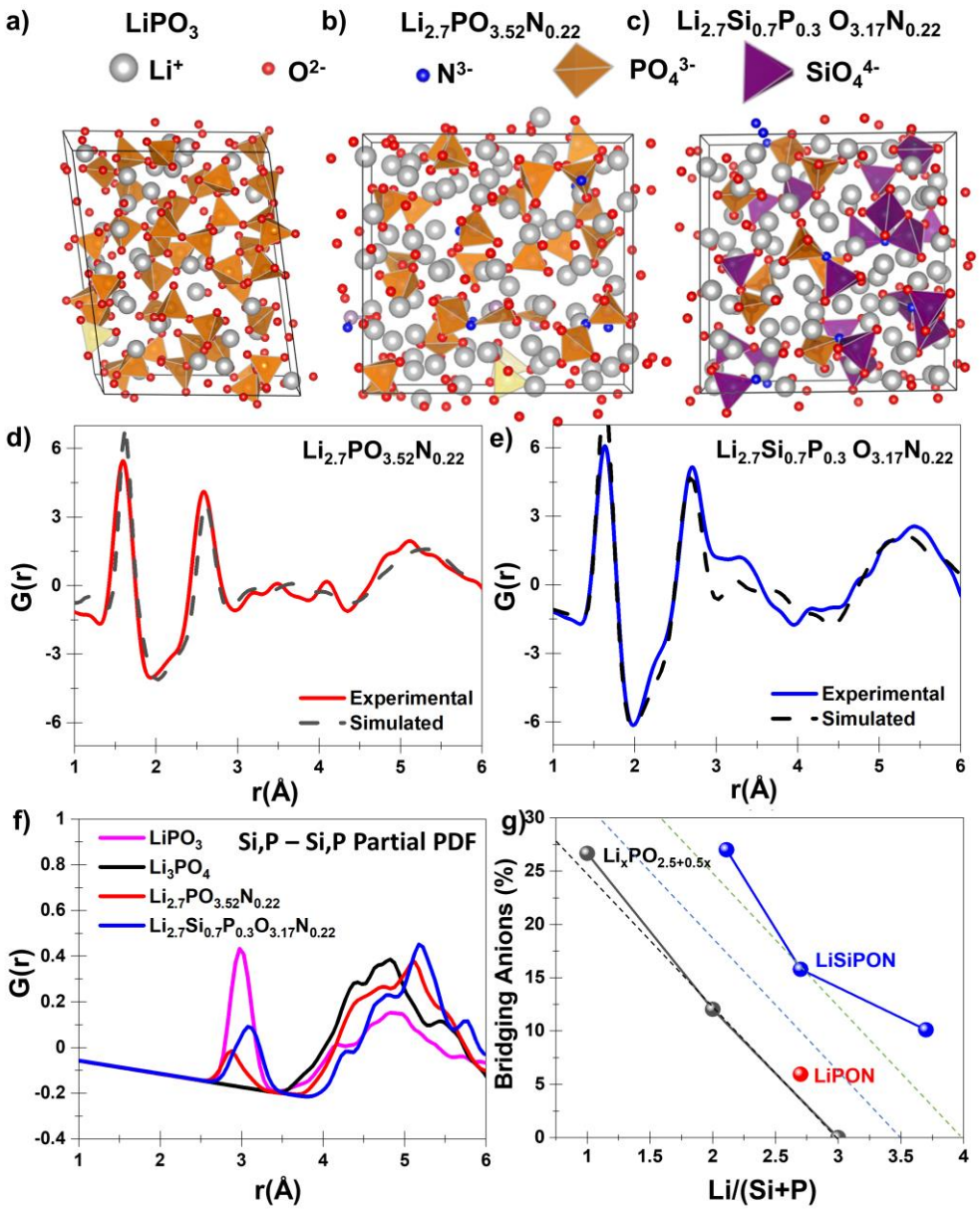

Figure 1. Simulated structures from AIMD models for amorphous (a) $LiPO_3$, (b) $Li_{2.7}PO_{3.52}N_{0.22}$ and (c) Li $Li_{2.7}Si_{0.7}P_{0.3}O_{3.17}N_{0.22}$. Comparison of simulated and experimental pair distribution functions from 1-6 Å for (d) $Li_{2.7}PO_{3.52}N_{0.22}$ and (e) Li $Li_{2.7}Si_{0.7}P_{0.3}O_{3.17}N_{0.22}$. (f) Partial pair distribution functions (a sum of Si-Si and P-P) for $LiPO_3$, Li_3PO_4, $Li_{2.7}PO_{3.52}N_{0.22}$ and Li $Li_{2.7}Si_{0.7}P_{0.3}O_{3.17}N_{0.22}$. (g) Percentage of bridging anions in all our simulated structures including $LiPO_3$, $Li_4P_2O_7$, Li_3PO_4, $Li_{2.7}PO_{3.52}N_{0.22}$, $Li_{2.11}Si_{0.66}P_{0.33}O_{2.93}N_{18}$, $Li_{2.7}Si_{0.7}P_{0.3}O_{3.17}N_{0.22}$, and $Li_{3.7}Si_{0.5}P_{0.5}O_{3.5}N_{0.4}$. The dashed lines represent the expected % of bridging anions for a given Li/(Si+P) ratio for pure Li_3PO_4 (black), mixed $Li_{3.5}Si_{0.5}P_{0.5}O_4$ (blue), and pure Li_4SiO_4 (green)

In summary, adding both Si and N to the Li_3PO_4 structure increases the number of bridging

anions for any given Li: Si+P ratio. This matches with the predicted structure as expected due to the lower oxidation state of Si (4+) compared to P (5+) and the difference between O (2-) and N (3-). The increased Li content paired with the increased number of bridges likely contributes to the improved ionic conductivity of LiSiPON over LiPON.

One question remaining from the previous work is if there is a way to experimentally identify the increased number of cation-anion-cation bridges between silicate or phosphate tetrahedra. The previous work by Lacivita *et al.* concluded that it was almost impossible to observe the differences due to the cation-anion-cation bridges based on neutron scattering. A look at the scattering cross sections makes this evident. Because of the relatively small number of Si and P cations, the P-O/Si-O and anion-anion pairs dwarf the signal from the cation/cation coordination, making the bridging anions' signature at 2.9 Å indistinguishable in the total PDF. We briefly experimented with the possibility of distinguishing the cation-cation peak from X-ray PDF as it is much more sensitive to atomic number. The number of anions, however, makes it difficult to distinguish the cation-cation peaks in X-ray PDF as well. A simulated X-ray PDF for LiPON is presented in Figure S3 of the supporting information. Likely additional experimental techniques which are more sensitive to the bond structure are needed to highlight this feature, such as Raman spectroscopy.

Building on our understanding of the local structure, we are now prepared to explore the medium-range ordering in the LiPON and LiSiPON structures. While the simulations provide a good deal of information on the local structure of the LiPON and LiSiPON, much of the information is limited to <9 Å. However, understanding the local ordering in LiPON and LiSiPON prepares us to evaluate and understand the medium-range ordering. Recent work by the Egami group has demonstrated that the medium-range structure of amorphous

materials can have a significant impact on various properties, including the mechanical properties.[23, 24] The full experimental scattering data $S(Q) - 1$ and the Fourier transformed pair distribution functions (PDF) for $LiPO_3$, $Li_{2.7}PO_{3.52}N_{0.22}$, and $Li_{2.7}Si_{0.7}P_{0.3}O_{3.17}N_{0.22}$ are presented in Figure 2. The $LiPO_3$ samples were made by a traditional melt quench where crystalline $LiPO_3$ powder was heated above the melting temperature in an alumina crucible and allowed to cool. The glass puck was then ground to a powder using ball milling. For the LiPON samples, we sputtered a Li_3PO_4 target in N_2 to a thickness of ~20 μm onto a Kapton film. The Kapton film was then bent, causing the LiPON film to fragment and delaminate. We then collected the resulting powder in a capillary and performed the neutron scattering. For the LiSiPON materials, we have recently developed an alternative plasma synthesis method using an inductive plasma torch.[25] This method produces spherical powders ~90 nm in diameter. These powders were loaded into another capillary. Using ICP of similar materials formed in the sputtering of LiPON, we estimate the composition to be $Li_{2.9}PO_{3.85}N_{0.40}$ for LiPON. For the LiSiPON, we produced three powders with different compositions, including $Li_{2.11}Si_{0.66}P_{0.33}O_{2.93}N_{18}$, $Li_{2.7}Si_{0.7}P_{0.3}O_{3.17}N_{0.22}$, and $Li_{3.7}Si_{0.5}P_{0.5}O_{3.5}N_{0.4}$ based on a combination of ICP-MS and EDX analysis.[25] These methods inherently have error involved, so there is likely variation in the composition, but these are reasonable approximations. This paper focuses on the melt-quenched $LiPO_3$, sputtered $Li_{2.9}PO_{3.85}N_{0.40,}$ and the plasma-produced $Li_{2.7}Si_{0.7}P_{0.3}O_{3.17}N_{0.22}$ powders. These powders were of the highest quality and were completely amorphous. This is evident in the scattering data in Figure 2. There are some very small crystalline peaks for $Li_{2.7}Si_{0.7}P_{0.3}O_{3.17}N_{0.22}$ arising from lithium carbonate on the

surface, but because of the low intensity they have virtually no impact on the final pair distribution function data. For more information see Figure S4.

In the $S(Q) - 1$ data for these materials, there are two distinct regions. The two sharp diffraction peaks from $1Å^{-1}$ - $4Å^{-1}$ in Q space correspond to the medium-range ordering in

Table 1 FSDP Analysis

Sample	S(Q) Peak Position ($Å^{-1}$)	FSDP Intensity	FWHM ($Å^{-1}$)	1st G(r) peak position (Å)	Periodicity (Å)
$LiPO_3$	1.55±0.01	0.12±0.01	0.67±0.01	5.03±0.03	4.03±0.03
$Li_{2.9}PO_{3.35}N_{0.40}$	1.562±0.003	0.50±0.05	0.33±0.05	5.03±0.01	4.03±0.01
$Li_{2.7}Si_{0.7}P_{0.3}O_{3.17}N_{0.22}$	1.59±0.01	0.15±0.03	0.39±0.03	4.94±0.10	3.95±0.08

Table 2 SSDP Analysis

Sample	S(Q) Peak Position ($Å^{-1}$)	SSDP intensity	FWHM ($Å^{-1}$)	1st G(r) peak position (Å)	Periodicity (Å)
$LiPO_3$	2.790±0.003	0.17±0.01	0.48±0.01	5.06±0.01	2.251±0.002
$Li_{2.9}PO_{3.35}N_{0.40}$	2.663±0.002	0.87±0.04	0.29±0.04	5.31±0.01	2.361±0.004
$Li_{2.7}Si_{0.7}P_{0.3}O_{3.17}N_{0.22}$	2.640±0.004	1.10±0.02	0.30±0.02	5.35±0.01	2.378±0.002

the material. In this publication, they will be referred to as the first sharp diffraction peak (FSDP) and second sharp diffraction peaks (SSDP). The second region > 4 $Å^{-1}$ corresponds to the local ordering that was the focus of the discussion centered around Figure 1. For $LiPO_3$, the first two S(Q) peaks corresponding to the mid-range ordering are broad, flat, and Gaussian, with peak intensities of 0.12 and 0.02, respectively. For $Li_{2.9}PO_{3.85}N_{0.40}$, both

peaks are sharper and more intense. The second sharp diffraction peak also approaches a Lorentzian shape. The peak intensities are 0.5 and 0.97, respectively. For $Li_{2.7}Si_{0.7}P_{0.3}O_{3.17}N_{0.22,}$ these two peaks are distinct from both the $LiPO_3$ and $Li_{2.9}PO_{3.85}N_{0.40}$ structures. For $Li_{2.7}Si_{0.7}P_{0.3}O_{3.17}N_{0.22,}$ the first peak is relatively low in intensity and Gaussian in shape. However, the second peak is sharp and more Lorentzian. The peak intensities are 0.15 and 1.10, respectively. In these systems, the FSDP corresponds to the phosphate/silicate tetrahedra substructure with an average periodicity of 4.03 Å, 4.03 Å, and 3.95 Å for $LiPO_3$, $Li_{2.9}PO_{3.85}N_{0.40,}$ and $Li_{2.7}Si_{0.7}P_{0.3}O_{3.17}N_{0.22}$ respectively (see Table 1). The SSDP corresponds to the O/N substructure with an average periodicity of 2.25 Å, 2.36 Å, and 2.38 Å for $LiPO_3$, $Li_{2.9}PO_{3.85}N_{0.40,}$ and $Li_{2.7}Si_{0.7}P_{0.3}O_{3.17}N_{0.22}$ respectively (see Table 2).

As the number of Li ions in the structure increases and the structure moves from a phosphate network structure to an inverted glass structure, the medium-range ordering of both the phosphate tetrahedra substructure and the O/N substructure increases substantially. When Si is substituted into the structure, the intensity of the FSDP decreases significantly, but the intensity of the SSDP increases significantly. The decrease in the intensity of the FSDP intuitively makes sense. When Si is substituted with the same Li: Si+P ratio, two things happen that can significantly disrupt the phosphate/silicate substructure. First, the silicate tetrahedra have slightly different bond lengths and a different polyanionic charge (4- as opposed to 3-). Second, the lower charge also results in a significant amount of bridging anions, so while it is still an inverted structure, there are many isolated tetrahedra and bridged dimer structures. The combination of both deviant structures will increase the disorder in the polyanion substructure resulting in the FSDP

intensity dropping. However, the increased intensity in the SSDP corresponding to the O/N substructure is surprising. As the phosphate/silicate network decreases in intensity, the intensity of the SSDP is enhanced. For details on the peak analysis, see Tables 1 and 2.

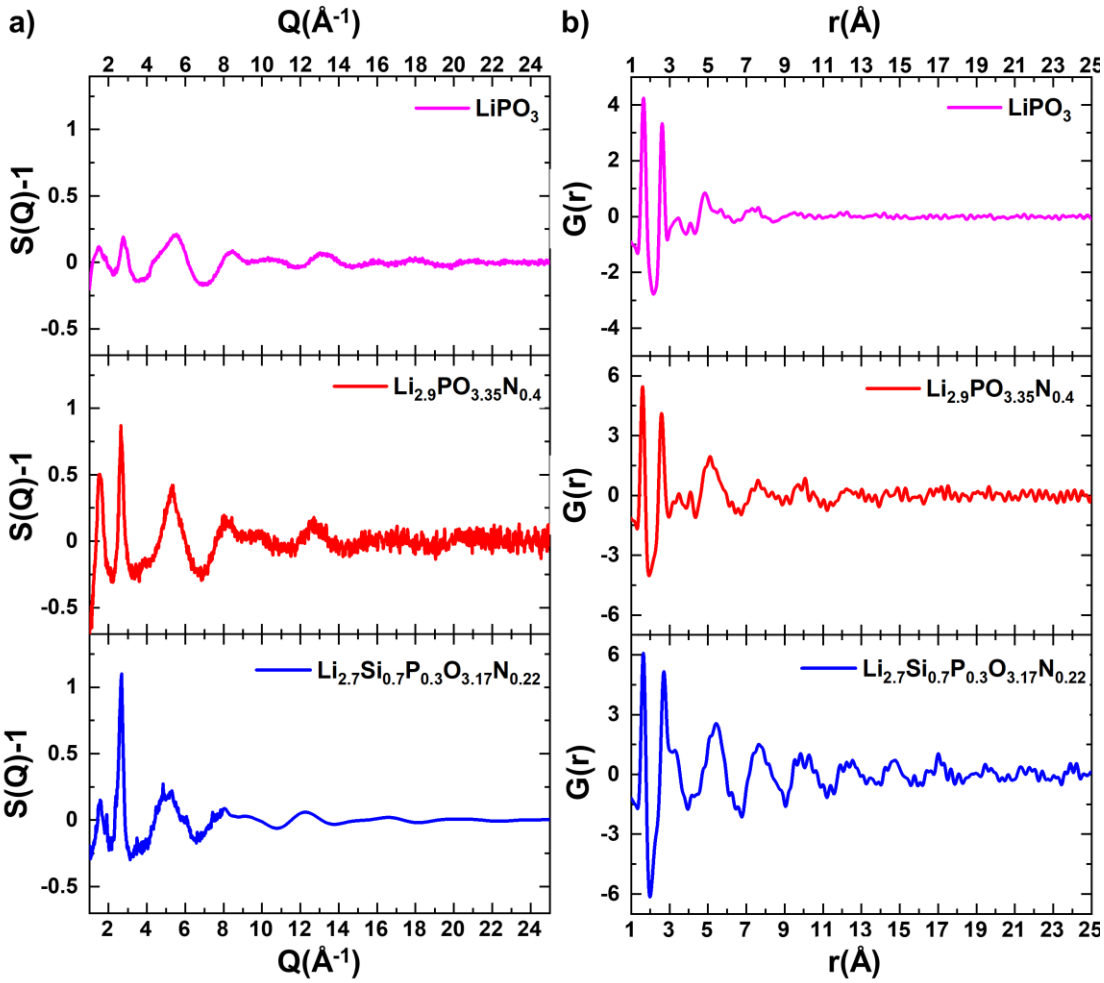

Figure 2. (a) Experimental neutrons scattering function S(Q)-1 for $LiPO_3$, $Li_{2.9}PO_{3.35}N_{0.4}$, and $Li_{2.7}Si_{0.7}P_{0.3}O_{3.17}N_{0.22}$. (b) Pair distribution functions for the neutron scattering data in (a).

Further insight is gained by performing the Fourier transform of the $S(Q)$ data to generate the PDF $G(r)$ data presented in Figure 2b. The $g(r)$ data is also presented in the supporting information in Figure S5. The local structure is similar in each case and discussed in detail above. What is most interesting is the medium-range ordering from 5-25 Å. In each

structure, we see evidence of the periodic oxygen sub-structure represented by the SSDP. For $LiPO_3$, this periodicity is distinct from the noise[26] until about 9 Å. The periodicity is ~2.2/2.3 Å in line with the calculated periodicity from the SSDP. For the $Li_{2.9}PO_{3.85}N_{0.40}$ structure, there is a periodic mid-range structure that is distinguishable from the background noise until about 14 Å with a periodicity of ~2.3 Å. For the $Li_{2.7}Si_{0.7}P_{0.3}O_{3.17}N_{0.22}$**,** the mid-range ordering is the most pronounced, with a distinct 2.3 Å periodicity extending to ~21 Å. This data is a direct reflection of the intensity and calculated periodicities of the SSDP.

This medium-range ordering can be seen more distinctly in Figure 3, which shows the $|G(r)|$. A line shows the exponential decay in the intensity of $G(r)$ as a function of radial distance. While the medium-range ordering of $LiPO_3$ quickly damps out, and the noise in the $Li_{2.9}PO_{3.85}N_{0.40}$ obscures the structure beyond about 9 Å, the $Li_{2.7}Si_{0.7}P_{0.3}O_{3.17}N_{0.22}$ medium-range ordering (MRO) is clear. It is visually illustrated with a dotted black line to guide the eye. To provide some additional depth, we fit the PDF data to the general formula below.[27]

$$g(r) - 1 \approx A_{MRO}\frac{a}{r}sin(Q_{MRO}r + \delta_{MRO})\,exp\left(-\frac{r}{\xi_s}\right), \quad r > r_{cutoff} \qquad (1)$$

In equation (1), A_{MRO} is the amplitude of the mid-range ordering oscillation, a is the nearest neighbor distance defined by the first maximum in the PDF, δ_{MRO} is the phase factor, r is the radial distance, and ξ_s is the structural coherence length which characterizes the medium-range ordering. While the fits for the $LiPO_3$ and $Li_{2.9}PO_{3.85}N_{0.40}$ were less than ideal, the fit for the $Li_{2.7}Si_{0.7}P_{0.3}O_{3.17}N_{0.22}$ was reasonable and gave a structural coherence length of 7.4 Å. These fits are presented in Figure S6.

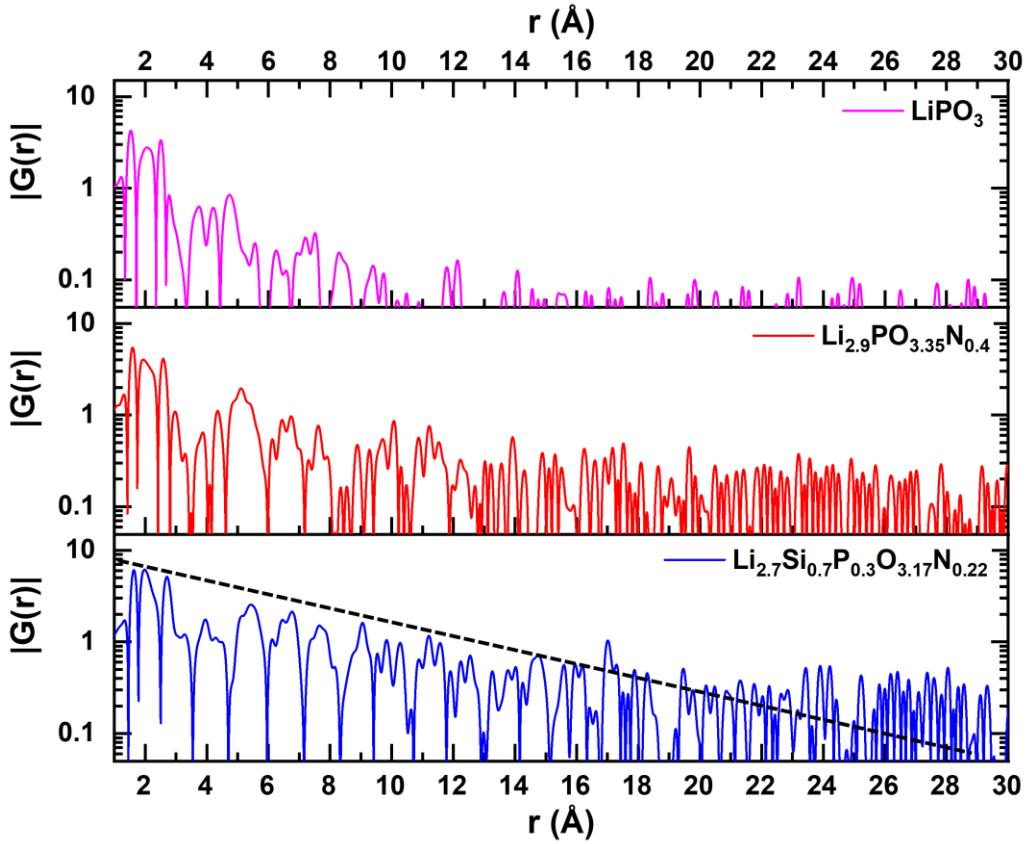

Figure 3. |G(r)| for $LiPO_3$, $Li_{2.9}PO_{3.35}N_{0.4}$ (LiPON), and $Li_{2.7}Si_{0.7}P_{0.3}O_{3.17}N_{0.22}$ (LiSiPON). The dashed line is included to guide the eye and is indicative of the coherence length.

The periodicity and structural coherence of the medium range ordering in these ionic glasses is comparable with that of both liquids and bulk metallic glasses. Recent theoretical work by Egami et al. has presented a framework describing ideal close-packed amorphous/liquid structures.[27-29] While these structures have no crystalline structure, as evidenced by Bragg peaks in X-ray and neutron scattering data, they can have a significant amount of medium-range ordering. In fact, an ideal close-packed amorphous material has an oscillation in the structural density function $G(r)$ that extends to infinity. The degree to which these amorphous structures have this medium-range ordering is a measure of how ideal the structures are. The structural coherence length is one measure that can give some sense of how ideal an amorphous structure is.[24] While this structural coherence or ideal

amorphous structures have been observed in liquids and metallic glasses; they have not previously been observed in amorphous oxides. One reason is that most amorphous oxides are traditional glasses characterized by extensive covalently bonded networks, often referred to as a continuous random network (CRN). The nature of these strong covalent bonds and the ability to form these extended network structures allows materials like SiO_2 and P_2O_5 to form amorphous structures readily, but they also preclude the possibility of forming an 'ideal' amorphous structure with dense-random-packing.[30] The electrolytes LiPON or LiSiPON fall into a special category of glasses called invert glasses or ionic glasses.[31] In these glasses, what is traditionally considered a network modifier, such as Li^+, becomes the dominant species in the material. The percentage of ionic bonds in these structures is significantly higher than in traditional glasses. Notably, ionic bonds are basically spherical and are much less rigid than covalent bonds allowing for greater flexibility in the orientation of the phosphate or silicate tetrahedra. Essentially the breakdown of a continuous random network opens the possibility of approaching an ideal glass.

Having grasped a sense of the structure of these amorphous materials, we would like to consider the potential impact on the ionic conductivity and mechanics. For ionic conductivity, there is a correlation between the ionic conductivity and the ideality of the structures, i.e., the ionic conductivity of $LiPO_3$ < $Li_{2.9}PO_{3.85}N_{0.40}$ < $Li_{2.7}Si_{0.7}P_{0.3}O_{3.17}N_{0.22}$. Glasses are spatially heterogeneous because of their random structures. However, the extent of spatial heterogeneity differs from one glass to another. A good measure to characterize this heterogeneity is the concept of "ideality," defined by the structural coherence length, ξ_s, defined by eq. (1).[26] The longer the ξ_s, the more ideal the glass

structure is with less heterogeneity. This coherence length is directional and related to the intensity of the FSDP and SSDP. It is tempting to speculate that higher structural heterogeneity results in stronger trapping of Li ions and thus in lower ionic mobility. In contrast, a more ideal glass is structurally less heterogeneous, more akin to crystalline superionic conductors, resulting in higher ionic mobility. While the direct conductivities of the materials used for neutron total scattering were not measured due to their powder form, surveys of the ionic conductivities of comparable thin films made by sputtering have are shown by Lacivita *et al.* for LiPON,[16] and by Framprikis et al. for LiSiPON. They reported maximum ionic conductivities of ~2.5 x 10^{-9} S/cm for $LiPO_3$ based compositions,[32] 3.3 x 10^{-6} S/cm for LiPON and 2 x 10^{-5} S/cm for LiSPON.[20] While there are clearly molecular differences that significantly contribute to the difference in ionic conductivity, it is worth considering what impact the medium range order may play.

One of the most accepted models for determining ion conduction in glasses is the Andersen-Stuart model.[33] There have been multiple studies that have demonstrated that for traditional glasses this model accurately predicts the activation energies for ion conduction in glasses albeit with some minor adjustments to the theory such as that proposed by Christiansen and Martin.[34-35] One of the underlying assumptions in this model is that in a fully amorphous material there is a distribution of activation energies for ion transport.[35] Because it is impossible to precisely know the locations of every atom in the structure relative to each other, this model relies on the assumption that there is no preferred path for ion conduction.[33] The calculated activation energy will therefore only match the average activation energy of the bulk glass. One possible effect of medium range order is the generation of a preferred paths for ion conduction known as percolation paths that

facilitate lower overall activation energy for ion conduction than the average activation energy predicted by the Andersen-Stuart model. Further research into ionic glasses will likely lead to a much greater understanding of the ability of ionic glasses to form ideal amorphous medium-range structures and the relationship with ionic conductivity.

The second property of interest is the elastic modulus. In metallic glasses, the amorphous structure directly impacts the modulus, including the ideality of structure.[23] From the literature, $LiPO_3$ has an elastic modulus of 48 GPa.[36] We obtained slightly higher value equal to 59 GPa by in-house measurements using nanoindentation of bulk metaphosphate $LiPO_3$. To measure these values for LiPON and LiSiPON, we sputtered thick LiPON from a Li_3PO_4 target, and LiSiPON films from a 40% Li_2SiO_3 / 60% Li_3PO_4 target sputtered in N_2 gas. While the exact LiSiPON composition is somewhat different than the powder analyzed above ($Li_{2.6}Si_{0.4}P_{0.6}O_{3.6-x}N_{2x/3}$), the Li: Si+P ratio the structure will be similar. We then performed nanoindentation on the films to measure the modulus. We measured moduli of 80 GPa for LiPON and 95 GPa for LiSiPON. Similar to the ionic conductivity, we can again see a correlation between the elastic modulus and the degree of medium range ordering as measured by the intensity of the SSDP. While this data is insufficient to draw conclusions, it suggests that the degree of ideality in the medium range ordering may directly affect the elastic modulus and other related properties.

The final property we want to explore briefly is the effect of the structure on the ductility of the materials as measured by nanoindentation. Our recent paper on the mechanics of LiPON has demonstrated that it plastically deforms under intense pressure from a cube-corner nanoindenter.[21] This is in direct contrast to traditional ceramics and glasses, which quickly form radial cracks under pressure from the nanoindenter. One key question is what

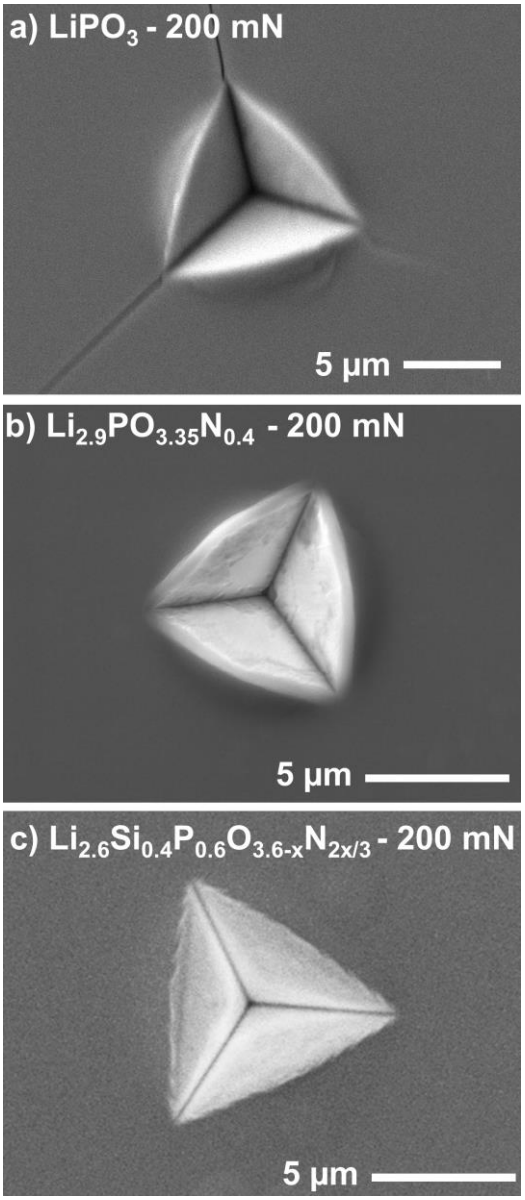

Figure 4. Residual hardness impressions after nanoindentation to P_{max} = 200 mN with cube corner nanoindenter tip: a) $LiPO_3$ metaphosphate glass a) $Li_{2.9}PO_{3.35}N_{0.4}$ (LiPON), b) $Li_{2.6}Si_{0.4}P_{0.6}O_{3.6-x}N_{2x/3}$ (LiSiPON)

compositional and structural factors result in the anomalous improvement in ductility. In our previous work, we included simulations that showed that the high alkali content plays a significant role in Li-containing phosphate glasses' ability to densify and plastically deform. At that time, the degree of medium-range ordering had not been demonstrated. It is also possible that the degree of medium range ordering also impacts the ductility. In metallic glasses, the increase in modulus associated with higher entropy often increases the brittleness of the structure. To give some additional insight into this mechanical behavior, we performed additional nanoindentation on LiPON and indented LiSiPON of the composition $Li_{2.6}Si_{0.4}P_{0.6}O_{3.6-x}N_{2x/3}$. These were the same films used to measure the elastic modulus. The residual hardness impressions are presented in Figure 4. We see significant plastic deformation and no evidence of radial cracking in both cases. Formation of radial cracks in $LiPO_3$ under the same load and strain rate is shown for comparison in Figure 4a.

As we only have a qualitative measure here, it is impossible to draw concrete conclusions. Nonetheless, the duplication of the ductility in the LiSiPON structure suggests that more research into the structure-property relationship in these ionic glasses will give significant insight into stiff ductile glasses.

CONCLUSION

The solid electrolytes LiPON and LiSiPON have a unique combination of properties, including ionic conductivity, lack of grains/grain boundaries, mechanical stiffness, and ductility on the 'dendrite' length scale. Here we have provided an in-depth exploration of the structure of LiPON and LiSiPON electrolytes to give some insight into their properties. The local ordering of these structures is characterized by a high Li content leading to an inverted ionic glass structure. This inverted structure consists of isolated or paired phosphate and silicate tetrahedra suspended in a Li^+ matrix. Adding both Si and N promotes the dimer or bridged phosphate/silicate tetrahedra, improving conductivity. In addition to this local short-range ordering, this inverted structure also gives rise to a distinct medium-range ordering. This medium-range ordering is characterized by an oscillating structural density function with a periodicity of about 2.3 Å. This medium-range ordering is characteristic of close packed/ideal amorphous ordering based on theoretical work on metallic glasses and liquids. These distinct structural features result in the amorphous ionic glass materials LiPON and LiSiPON having a unique combination of high ionic conductivity, mechanical stiffness, and mechanical ductility.

COMPUTATIONAL METHODS

Dynamics and generation of amorphous structures

All dynamics calculations used density-functional theory using a plane-wave basis (400 eV cutoff) and periodic boundary conditions. Simulations used the Vienna Ab-Initio Simulation Package (VASP)[37-39] with a generalized gradient PBE functional[40]and projected augmented wave (PAW) pseudopotentials.[41] The reciprocal-space integration was Γ-only due to the large cells. The dynamics had a time step of 2 fs because the lightest element is Li, using a Nosé–Hoover thermostat.[42]

Amorphous structures were generated with the standard melt-quench technique with convergence testing. The initial structure was a $Li_wP_xSi_yO_z$ crystal; after testing, the exact structure was not sensitive; as long as it contained at least ~200 atoms, it converged to the same elementwise radial distribution functions after the melt-quench procedure. Due to computational constraints, the cell was therefore limited to ~10-15Å per lattice vector. The crystal was melted at 3000 K for 50 ps, preceded and followed by a zero-temperature relaxation of the cell shape and volume to account for pressure from the amorphous phase. The material was then immediately quenched at 600 K for a further 50 ps.

The radial distribution functions (RDF) were converted to reciprocal space with the standard equation $G(r) \propto r[g(r) - 1] \propto \int [S(q) - q]q \sin qr \, dq$ (omitting a normalization constant), where g(r) is the probability of a pair of atoms being separated by a distance r, and S(q) is the neutron scattering measurement (sometimes reported as S(q)-1). The simulated neutron amplitudes were calculated assuming a 0% Li-6 content. The computed RDF were averaged over several ps of snapshots.

EXPERIMENTAL METHODS

Materials preparation

LiPON films for experimental PDF were made by sputtering using a homemade target. To enhance the signal, isotopically pure (Li-7) OH and H_3PO_4 were combined in 18 MΩ water in a 3:1 molar ratio. The subsequent reaction resulted in the precipitation of $(Li\text{-}7)_3PO_4$. The $(Li\text{-}7)_3PO_4$ powder was then pressed into a 2.5-inch disk about ~1/4 inch thick. The pressed target was then sintered at 1000˚C. After the sintering, the target was bonded to a 2" Cu backing plate. Cr, Ni, and Au were sputtered sequentially to perform the bonding. After the sputtering, the backing plate and the target were sandwiched together and heated to 350ºC in a retort furnace with a 1 kg weight on top for 45 minutes. The resulting target was used to sputter LiPON films in an N_2 plasma at a power of 100W, a flow rate of 20 SCCM, and a working pressure of 20 mT. The base pressure was below 3×10^{-6} S/cm.[16] To capture enough material for a high-quality pair distribution function measurement, a flexible Kapton film was attached with an area of approximately 6" x 6". We sputtered the film until it was over 20 µm thick at a rate of ~30 Å/min. After the deposition, we bent and crinkled the LiPON-coated Kapton causing the LiPON to delaminate (mostly in a powder form). We captured the delaminated LiPON and poured it into a capillary. The powder filled capillary was then quickly moved to an Ar glove box to limit reactions with air. The capillary was sealed in an Ar glove box before transportation to the beamline for neutron scattering experiments. LiPON films for mechanical measurements used the same sputtering process to similar thicknesses but used a 2" elastomer bonded Li_3PO_4 target using natural Li purchased from Kurt J. Lesker Company. The LiSiPON films for the mechanical measurements were sputtered using a 2" target with a mixed composition of

40% Li_2SiO_3-60% Li_3PO_4 on a Cu backing plate purchased from Toshima LLC. The sputtering conditions were the same as for LiPON with an N_2 flow rate of 20 SCCM, a working pressure of 20 mT, a base pressure of $<3 \times 10^{-6}$ Torr, and a deposition power of 90W. For the mechanical measurements, polished sapphire was used as the substrate.

For the LiSiPON powder used for the neutron PDF, we used an alternative plasma processing. The detailed methods are described in another paper.[25] In summary, a mixture of $Li_4P_2O_7$, Si_3N_4, and Li_2O were propelled through an induction plasma torch using a Tekna induction plasma torch with the Teknano reactor attached to form an amorphous nanopowder. This nanopowder has an ionic conductivity of 7×10^{-7} S/cm when cold pressed and has an average diameter of ~90 nm. To prevent he nanopowder from being affected by reactions with water and CO_2 in the air, the powders were transferred from the Teknano reactor to an Ar glovebox. The powder was also carefully loaded into dried glass capillary in an Ar glove box to limit air exposure. The capillaries were designed with a cap and seal to minimize air exposure while transporting to the beamline. To further minimize the risk of air contamination, the transfer of the samples to the beamline was coordinated to minimize the time the sealed capillary spent in the ambient environment.

$LiPO_3$ glass ingots made for nanoindentation were made as follows. Lithium metaphosphate, $LiPO_3$, was prepared from stoichiometric amounts of Li_2CO_3 (Alfa Aesar 99%) and $(NH_4)_2HPO_4$ (Acros 99+%). The compounds were mixed in a large mortar and pestle, transferred to a porcelain crucible, and placed into a furnace. The furnace was heated at a rate of 1°C/min from 25°C to 200°C, held for 4 hours at 200°C, heated to 600°C, held for 4 hours at 600°C to promote the removal of CO_2, NH_3, and H_2O, heated to 800°C and held for at least 2 hours. The melt was then quenched to room temperature onto a brass

mold and stored in a glovebox. The pellets were then polished to prepare the surface for nanoindentation.

Compositional characterization

Compositional characterization of the LiPON was performed on LiPON films made with the same methodology, although they were different films. LiSiPON powders were directly used. In both cases, the material was dissolved in Aqua Regia and then diluted with pure water (18MΩ). The resultant solutions were analyzed with a Thermo Scientific iCAP 7400 ICP-OES Duo. Calibrations for the different elements were performed using TraceCert ICP standards purchased from Sigma-Aldrich. The standards were diluted from the initial 1000 ppm solutions to 50, 20, 10, 5, 2, and 1 ppm. These calibration standards were used to obtain the relative concentrations of Li, P, and Si. Ratios of P, Si to N were obtained from EDX analysis from a TM3030 Plus tabletop microscope. O was determined by charge balancing.[16, 25]

Neutron PDF data and analysis

The Neutron total scattering data were collected at the NOMAD beamline at the Spallation Neutron Source (SNS) at Oak Ridge National Laboratory (ORNL). The samples were synthesized as described in the previous section. The obtained powders were loaded into quartz capillaries in an Ar-filled glove box for the scattering measurements. The capillaries used an ORNL design to minimize air exposure. The samples were further loaded into a 50 mL centrifuge tube and further sealed to minimize air exposure. Background data was obtained from an empty quartz capillary and subtracted from the data. The data were normalized using scattering data from a 6 mm vanadium rod. No absorption correction was applied. Analysis of the *S(Q)* first and second sharp diffraction peaks (FSDP and SSDP)

included the peak position, peak height, the full width half maximum (FWHM), the location of the first peak in the Fourier transformed *g(r)* data and the periodicity of the medium range ordering. The periodicity ω was calculated using $\omega = 2\pi/q$ where q is the peak position in the *S(Q)* data. The first peak location r_0 was calculated using the equation $r_0 = 5\pi/2q$. The Fourier transform *g(r)* of the scattering data *S(Q)* employed a maximum Q of 25 $Å^{-1}$ and utilized the Lorch function to minimize noise. *g(r)* data was translated to *G(r)* using the equation

$$G(r) = \pi \rho_0 r(g(r) - 1)$$

where *r* is the radial distance in Å and ρ_0 is the atomic density. The atomic densities were calculated from the simulations with values of 0.080, 0.092, and 0.089 atoms/$Å^3$ for $LiPO_3$, $Li_{2.7}PO_{3.52}N_{0.22}$, and $Li_{2.7}Si_{0.7}P_{0.3}O_{3.17}N_{0.22}$ respectively. The errors were obtained as follows. For the peak position, peak centers and associated errors were determined with a Voight fit to the FFSD and SSDP. For the intensity data the error resultant from the PDF measurement was used. Error for the FWHM, 1st G(r) peak position, and Periodicity were determined using error propagation.

Nanoindentation

Nanoindentation experiments on LiPON and LiSiPON films were performed using InForce 1000 actuator by NanoMechanics Inc. The actuator mounted on the frame was installed inside the TESCAN Mira 3 SEM to observe the indentation process. The nanoindentations were performed with a diamond cube corner nanoindenter tip $\alpha = 35.26^o$ supplied by Micro Star Technologies. All the experiments were conducted at room temperature. The cube corner nanoindenter tip induces a nominal strain of 22% and is recommended for

measuring the micro-scale fracture toughness of glass and ceramics. The maximum load was kept at 200 mN in the experiments.

ASSOCIATED CONTENT

Supporting Information

The Supporting Information is available free of charge on the ACS Publications website at DOI: 10.1021/jacs.8b00277. Supporting information includes a comparison of the simulated and experimental PDF for $LiPO_3$ from 1-6 Å, simulated partial PDF data of $Li_{2.7}Si_{0.7}P_{0.3}O_{3.17}N_{0.22}$, simulated X-ray PDF of $Li_{2.7}PO_{3.52}N_{0.22}$, a comparison of LiSiPON scattering data with and without air exposure, unweighted PDF data *g(r)* for all three compositions, and fitting of the mid-range ordering of the three key compositions.

ACKNOWLEDGEMENTS

The authors would like to acknowledge the support of Paul Albertus at ARPA-E. Funding for this work was primarily provided by ARPA-E Award # 00000775. A portion of this research used resources at the Spallation Neutron Source, a DOE Office of Science User Facility operated by the Oak Ridge National Laboratory. TE was supported by the U. S. Department of Energy, Office of Science, Basic Energy Sciences, Materials Science and Engineering Division.

This manuscript has been authored by UT-Battelle, LLC, under contract DE-AC05-00OR22725 with the US Department of Energy (DOE). The US government retains and the publisher, by accepting the article for publication, acknowledges that the US government retains a nonexclusive, paid-up, irrevocable, worldwide license to publish or reproduce the published form of this manuscript, or allow others to do so, for US

government purposes. DOE will provide public access to these results of federally sponsored research in accordance with the DOE Public Access Plan (http://energy.gov/downloads/doe-public-access-plan). Funding for this work was provided by ARPA-E Award No. DE-AR0000775. Support for Neutron scattering experiments was provided through a Spallation Neutron Source User Proposal IPTS 19271.1.

REFERENCES

1. Thorpe, M. F.; Tichý, L., *Properties and applications of amorphous materials*. Springer Science & Business Media: 2012; Vol. 9.
2. Hufnagel, T. C., Finding order in disorder. *Nature materials* **2004,** *3* (10), 666-667.
3. Pye, L. D.; Fréchette, V. D.; Kreidl, N. J., *Borate glasses: structure, properties, applications*. Springer Science & Business Media: 2012; Vol. 12.
4. Görlich, E., The structure of SiO2—Current views. *Ceramics International* **1982,** *8* (1), 3-16.
5. Ketkaew, J.; Yamada, R.; Wang, H.; Kuldinow, D.; Schroers, B. S.; Dmowski, W.; Egami, T.; Schroers, J., The effect of thermal cycling on the fracture toughness of metallic glasses. *Acta Materialia* **2020,** *184*, 100-108.
6. Egami, T.; Iwashita, T.; Dmowski, W., Mechanical properties of metallic glasses. *Metals* **2013,** *3* (1), 77-113.
7. Dudney, N. J., Addition of a thin-film inorganic solid electrolyte (Lipon) as a protective film in lithium batteries with a liquid electrolyte. *Journal of Power Sources* **2000,** *89* (2), 176-179.
8. Yu, X.; Bates, J.; Jellison Jr, G.; Hart, F., A stable thin-film lithium electrolyte: lithium phosphorus oxynitride. *Journal of the electrochemical society* **1997,** *144* (2), 524.
9. Bates, J.; Dudney, N.; Gruzalski, G.; Zuhr, R.; Choudhury, A.; Luck, C.; Robertson, J., Fabrication and characterization of amorphous lithium electrolyte thin films and rechargeable thin-film batteries. *Journal of power sources* **1993,** *43* (1-3), 103-110.
10. Neudecker, B.; Dudney, N.; Bates, J., "Lithium-Free" Thin-Film Battery with In Situ Plated Li Anode. *Journal of the Electrochemical Society* **2000,** *147* (2), 517.
11. Westover, A. S.; Dudney, N. J.; Sacci, R. L.; Kalnaus, S., Deposition and confinement of Li metal along an artificial lipon–lipon interface. *ACS Ener. Lett.* **2019,** *4* (3), 651-655.
12. Li, J.; Ma, C.; Chi, M.; Liang, C.; Dudney, N. J., Solid electrolyte: the key for high-voltage lithium batteries. *Adv. Ener. Mat.* **2015,** *5* (4), 1401408.

13. Fleutot, B.; Pecquenard, B.; Martinez, H.; Letellier, M.; Levasseur, A., Investigation of the local structure of LiPON thin films to better understand the role of nitrogen on their performance. *Solid state ionics* **2011,** *186* (1), 29-36.
14. Muñoz, F.; Ren, J.; van Wüllen, L.; Zhao, T.; Kirchhain, H.; Rehfuß, U.; Uesbeck, T., Structure and Dynamics of LiPON and NaPON Oxynitride Phosphate Glasses by Solid-State NMR. *J. Phys. Chem. C* **2021,** *125* (7), 4077-4085.
15. Marple, M. A.; Wynn, T. A.; Cheng, D.; Shimizu, R.; Mason, H. E.; Meng, Y. S., Local structure of glassy lithium phosphorus oxynitride thin films: a combined experimental and ab initio approach. *Angewandte Chemie International Edition* **2020,** *59* (49), 22185-22193.
16. Lacivita, V.; Westover, A. S.; Kercher, A.; Phillip, N. D.; Yang, G.; Veith, G.; Ceder, G.; Dudney, N. J., Resolving the amorphous structure of lithium phosphorus oxynitride (Lipon). *J. Amer. Chem. Soc.* **2018,** *140* (35), 11029-11038.
17. Lacivita, V.; Artrith, N.; Ceder, G., Structural and compositional factors that control the li-ion conductivity in LiPON electrolytes. *Chem. Mater.* **2018,** *30* (20), 7077-7090.
18. Lee, S.-J.; Bae, J.-H.; Lee, H.-W.; Baik, H.-K.; Lee, S.-M., Electrical conductivity in Li–Si–P–O–N oxynitride thin-films. *Journal of power sources* **2003,** *123* (1), 61-64.
19. Su, Y.; Falgenhauer, J.; Leichtweiß, T.; Geiß, M.; Lupó, C.; Polity, A.; Zhou, S.; Obel, J.; Schlettwein, D.; Janek, J., Electrochemical properties and optical transmission of high Li+ conducting LiSiPON electrolyte films. *physica status solidi (b)* **2017,** *254* (2), 1600088.
20. Famprikis, T.; Galipaud, J.; Clemens, O.; Pecquenard, B.; Le Cras, F. d. r., Composition dependence of ionic conductivity in LiSiPO (N) thin-film electrolytes for solid-state batteries. *ACS Appl. Ener. Mat.* **2019,** *2* (7), 4782-4791.
21. Kalnaus, S.; Westover, A. S.; Kornbluth, M.; Herbert, E.; Dudney, N. J., Resistance to fracture in the glassy solid electrolyte Lipon. *J. Mat. Res.* **2021,** *36* (4), 787-796.
22. Herbert, E. G.; Tenhaeff, W. E.; Dudney, N. J.; Pharr, G., Mechanical characterization of LiPON films using nanoindentation. *Thin Solid Films* **2011,** *520* (1), 413-418.
23. Moon, J.; Egami, T., Enhancing elastic properties of single element amorphous solids through long-range interactions. *App. Phys. Lett.* **2021,** *119* (5), 051901.
24. Ryu, C. W.; Egami, T., Origin of liquid fragility. *Phys. Rev. E* **2020,** *102* (4), 042615.
25. Westover, A. S.; Kercher, A. K.; Kornbluth, M.; Naguib, M.; Palmer, M. J.; Cullen, D. A.; Dudney, N. J., Plasma synthesis of spherical crystalline and amorphous electrolyte nanopowders for solid-state batteries. *ACS App. Mat. & Int.* **2020,** *12* (10), 11570-11578.
26. Toby, B.; Egami, T., Accuracy of pair distribution function analysis applied to crystalline and non-crystalline materials. *Acta Crystallographica Section A: Foundations of Crystallography* **1992,** *48* (3), 336-346.
27. Egami, T.; Ryu, C. W., Medium-range atomic correlation in simple liquids. II. Theory of temperature dependence. *Phys. Rev. E* **2021,** *104* (6), 064110.
28. Ryu, C. W.; Dmowski, W.; Egami, T., Ideality of liquid structure: A case study for metallic alloy liquids. *Phys. Rev. E* **2020,** *101* (3), 030601.

29. Ryu, C. W.; Egami, T., Medium-range atomic correlation in simple liquids. I. Distinction from short-range order. *Phys. Rev. E* **2021,** *104* (6), 064109.
30. Bernal, J. D., A geometrical approach to the structure of liquids. *Nature* **1959,** *183* (4655), 141-147.
31. Calahoo, C.; Wondraczek, L., Ionic glasses: Structure, properties and classification. *J. Non-Cry. Sol. X* **2020,** *8*, 100054.
32. Wheaton, J.; Kmiec, S.; Schuler, D.; Sorensen, C.; Martin, S. W., Electrochemical Behavior of Drawn Thin-Film Vitreous Lithium Metaphosphate. *ACS Appl. Ener. Mat.* **2021,** *4* (10), 10835-10842.
33. Anderson, O.; Stuart, D., Calculation of activation energy of ionic conductivity in silica glasses by classical methods. *Journal of the American Ceramic Society* **1954,** *37* (12), 573-580.
34. Christensen, R.; Olson, G.; Martin, S. W., Ionic conductivity of mixed glass former 0.35 Na2O+ 0.65 [x B2O3+(1−x) P2O5] glasses. *J. Phys. Chem. B* **2013,** *117* (51), 16577-16586.
35. Kmiec, S.; Olson, M.; Kenney, M.; Martin, S. W., Interpretation of the Na+ Ionic Conductivity in Na4P2S7−x O x Mixed Oxy-Sulfide Glasses: Effects of Oxygen Doping. *Chem. Mater.* **2022**, 34 (21), 9479-9491.
36. Sokolov, I.; Valova, N.; Tarlakov, Y. P.; Pronkin, A., Electrical Properties and the Structure of Glasses in the Li2SO4–LiPO3 System. *Glass physics and chemistry* **2003,** *29* (6), 548-554.
37. Kresse, G.; Hafner, J., Ab initio molecular dynamics for liquid metals. *Phy. Rev. B* **1993,** *47* (1), 558.
38. Kresse, G.; Furthmüller, J., Efficiency of ab-initio total energy calculations for metals and semiconductors using a plane-wave basis set. *Computational materials science* **1996,** *6* (1), 15-50.
39. Kresse, G.; Furthmüller, J., Efficient iterative schemes for ab initio total-energy calculations using a plane-wave basis set. *Physical review B* **1996,** *54* (16), 11169.
40. Perdew, J. P.; Burke, K.; Ernzerhof, M., Generalized gradient approximation made simple. *Physical review letters* **1996,** *77* (18), 3865.
41. Kresse, G.; Joubert, D., From ultrasoft pseudopotentials to the projector augmented-wave method. *Phy. Rev. B* **1999,** *59* (3), 1758.
42. Nosé, S., A unified formulation of the constant temperature molecular dynamics methods. *J. Chem. Phys.* **1984,** *81* (1), 511-519.